Global Patterns of Submesoscale Surface Salinity Variability

KYLA DRUSHKA AND WILLIAM E. ASHER

Applied Physics Laboratory, University of Washington, Seattle, Washington

JANET SPRINTALL, SARAH T. GILLE, AND CLIFFORD HOANG

Scripps Institution of Oceanography, University of California, San Diego, La Jolla, California

(Manuscript received 22 January 2019, in final form 17 April 2019)

ABSTRACT

Surface salinity variability on $O(1–10)$ km lateral scales (the submesoscale) generates density variability and thus has implications for submesoscale dynamics. Satellite salinity measurements represent a spatial average over horizontal scales of approximately 40–100 km but are compared to point measurements for validation, so submesoscale salinity variability also complicates validation of satellite salinities. Here, we combine several databases of historical thermosalinograph (TSG) measurements made from ships to globally characterize surface submesoscale salinity, temperature, and density variability. In river plumes; regions affected by ice melt or upwelling; and the Gulf Stream, South Atlantic, and Agulhas Currents, submesoscale surface salinity variability is large. In these regions, horizontal salinity variability appears to explain some of the differences between surface salinities from the Aquarius and SMOS satellites and salinities measured with Argo floats. In other words, apparent satellite errors in highly variable regions in fact arise because Argo point measurements do not represent spatially averaged satellite data. Salinity dominates over temperature in generating submesoscale surface density variability throughout the tropical rainbands, in river plumes, and in polar regions. Horizontal density fronts on 10-km scales tend to be compensated (salinity and temperature have opposing effects on density) throughout most of the global oceans, with the exception of the south Indian and southwest Pacific Oceans between 20° and 30°S, where fronts tend to be anticompensated.

1. Introduction

Salinity varies over a range of horizontal scales due to oceanic dynamics and surface forcing from river runoff, evaporation, precipitation, and freezing/thawing of ice. The primary focus of this paper is submesoscale (defined here as smaller than 20 km) horizontal surface salinity variability, which affects density variability and therefore ocean dynamics. Submesoscale density fronts are often associated with strong vertical velocities in the mixed layer and thus can drive exchange of gases, salt, heat, carbon, and nutrients between the surface and the thermocline (e.g., Lévy et al. 2001; Lapeyre and Klein 2006; Thomas et al. 2008; Klein et al. 2015). Submesoscale density fronts can occur as a result of gradients in salinity or temperature, or both. Collocated temperature and salinity fronts can have opposing effects on density, so that although there are gradients in both properties, density remains approximately constant across the fronts. The weak density signature across these ''compensated fronts'' makes them more stable, allowing them to persist. In contrast, noncompensated density fronts with large density gradients tend to slump due to gravity, which increases mixing, and hence they have shorter lifetimes (Rudnick and Ferrari 1999; Rudnick and Martin 2002).

Salinity variations on scales < 100 km (i.e., the submesoscale to mesoscale regimes) impact interpretation of salinity measurements from satellite-based microwave radiometers [Aquarius, Soil Moisture and Ocean Salinity (SMOS), and Soil Moisture Active Passive (SMAP)]. These remote sensing measurements are typically validated with in situ data from Argo floats, moorings, and surface drifters. After atmospheric effects have been removed, radiometers provide the microwave brightness temperature of the top centimeter of the ocean that is the weighted spatial average over the radiometer ground footprint (~40–100 km across depending on the satellite). In contrast, in situ measurements are made at a single point and typically at a depth between 0.5 and 5 m, at least

Corresponding author: Kyla Drushka, kdrushka@apl.uw.edu

DOI: 10.1175/JPO-D-19-0018.1

an order of magnitude deeper than the satellite measurement. If the in situ sensor samples a point that does not represent the spatially averaged value of the satellite due to vertical and/or horizontal salinity variability, this causes a mismatch between the satellite and in situ salinity measurements, leading to apparent errors in the satellite products (Boutin et al. 2016). While the impact of the vertical salinity structure (e.g., due to rainfall-induced near-surface stratification or evaporatively formed salinity gradients) has been studied (e.g., Henocq et al. 2010; Boutin et al. 2014; Drucker and Riser 2014; Asher et al. 2014a,b; Tang et al. 2014; Drushka et al. 2016), there have been fewer investigations into the implications of horizontal variability (Lagerloef et al. 2010; Maes et al. 2013; Vinogradova and Ponte 2013).

The first objective of this work is to characterize submesoscale sea surface salinity variability, including changes in variability in each ocean basin, processes that generate variability, and the impact of salinity variability on density. The second objective is to determine where salinity variations smaller than the spatial footprint of satellite radiometers can contribute to apparent errors in satellite salinity. We combine measurements from several databases of thermosalinograph (TSG) data to obtain near-global coverage of surface temperature and salinity measurements at 2.5-km horizontal resolution. We also examine errors and uncertainties in the sea surface salinity measured by the Aquarius, SMAP, and SMOS satellite missions based on this near-global salinity database.

2. Background

Drivers of submesoscale sea surface salinity (SSS) variability include stirring by mesoscale eddies (e.g., Legal et al. 2007; Pietri et al. 2013) and turbulence (Després et al. 2011a) near large-scale salinity gradients; precipitation (e.g., Reverdin et al. 2012; Maes et al. 2013); riverine freshwater input (e.g., Brando et al. 2015); upwelling (Capet et al. 2008); ice–ocean–atmosphere interaction (Backhaus and Kämpf 1999; Manucharyan and Thompson 2017); and nonlinear buoyant adjustment to external forcing (Soloviev and Lukas 1997). Where and when these processes drive salinity variability, and the spatial and temporal scales of the salinity gradients they produce, remain open questions. A number of studies have used TSG measurements from voluntary observing ships to characterize regional SSS variability (Delcroix et al. 2005; Després et al. 2011b; Maes et al. 2013; Kolodziejczyk et al. 2015; Sena Martins et al. 2015). Consistent with the hypothesis that different processes can create horizontal variability in salinity, these studies demonstrate that submesoscale salinity fronts can exist over a range of geographic locations having different local atmospheric and ocean conditions and forcing mechanisms.

a. *Implications of submesoscale salinity variability for ocean dynamics*

Salinity and temperature control seawater density, so variability in density is driven by variability in either or both properties. Submesoscale density fronts slump due to gravity, energizing mixed layer instabilities and causing the mixed layer to stratify (Boccaletti et al. 2007; D'Asaro et al. 2011; Thompson et al. 2016). Submesoscale dynamics generate strong vertical velocities in the mixed layer, transporting dissolved gases, salt, heat, inorganic/organic carbon, and nutrients between the ocean surface and the base of the thermocline (e.g., Lévy et al. 2001; Thomas et al. 2008). However, much of our current understanding of submesoscale dynamics is derived from idealized numerical simulations over small spatial scales (e.g., Capet et al. 2008) or from high-resolution ocean general circulation models (e.g., Menemenlis et al. 2014), with in situ data available from only a handful of localized process studies (e.g., Hosegood et al. 2008; Shcherbina et al. 2015; Thompson et al. 2016; Ramachandran et al. 2018). As the spatial resolution of global-scale models improves so as to better resolve the submesoscale range, ensuring that the details of the model physics are accurately described becomes important. This motivates an observations-based approach to characterize submesoscale ocean physics. To our knowledge, a global observational characterization of the prevalence of submesoscale density variability, and its relation to salinity and temperature variability, has not been undertaken.

Submesoscale density fronts at the sea surface are often associated with strong vertical velocities in the mixed layer (e.g., Thomas et al. 2008), so understanding where density variability is strong and whether it is caused by temperature and/or salinity is important in understanding upper-ocean mixing. On scales smaller than the Rossby deformation radius for the mixed layer, density fronts tend to slump due to gravity, with the isopycnals tilting from the vertical to the horizontal, which disperses the fronts (Rudnick and Martin 2002). In contrast, compensated salinity/temperature fronts for which there is little change in density are not subject to slumping and hence are expected to persist (Rudnick and Ferrari 1999; Rudnick and Martin 2002). Rudnick and Ferrari (1999) showed that these compensated salinity/temperature fronts in the ocean mixed layer are ubiquitous on submesoscale distances from 20 m to 10 km, with horizontal temperature and salinity gradients canceling each other out to produce a nearly uniform density field. If only SST (or SSS) measurements are available, the picture of the

density variability could thus be incomplete and potentially misleading. Rudnick and Martin (2002) showed that compensated fronts are found in all ocean basins on 3–4-km scales, particularly when mixed layers are relatively deep, but they did not examine spatial patterns of compensation on regional scales within each basin. Making a consistent global estimate of submesoscale variability globally is challenging. Remote sensing of salinity and temperature can provide spatially extensive sampling, but there are issues with each in terms of resolving submesoscale variability. Satellite salinity measurements do not have high enough spatial resolution to capture submesoscale salinity variability (see below). In contrast, although satellite-mounted infrared imagers have high enough spatial resolution to capture submesoscale variability in SST, it is not clear whether or where SST alone dominates submesoscale density. In addition, high-resolution SST data are available only in clear-sky conditions, which are linked to downwelling solar radiation, so satellite-derived estimates of SST variability might be biased if variability is correlated with downwelling solar radiation.

b. *Implications of submesoscale to mesoscale surface salinity variability for satellite validation*

L-band radiometers measure salinity as a weighted spatial average over a large footprint: for satellite instruments, these footprints are approximately 45 km for SMOS, 40 km for SMAP, and 80–100 km for Aquarius (Boutin et al. 2016; Meissner et al. 2017). However, the area-averaged satellite salinity measurements are typically validated with in situ observations that represent salinity at a single point inside the footprint of the radiometer. In the presence of strong salinity variability on spatial scales smaller than one satellite footprint (i.e., submesoscales to mesoscales), the spatially averaged satellite data can potentially disagree with in situ point measurements. This disagreement would not be due to errors or bias in the satellite measurement, but because the spatial scales of the satellite sampling are so different from the in situ sampling.

Lagerloef et al. (2010) estimated the impact of spatial averaging on Aquarius salinity uncertainties by comparing raw ship-based TSG measurements to TSG measurements smoothed with a 150-km Gaussian filter. The difference, representing the uncertainty in Aquarius measurements due to comparison with point salinity measurements, was typically smaller than 0.1 psu except in strong frontal regions such as the Gulf Stream, where the difference approached 1 psu.

Using output from a numerical simulation, Vinogradova and Ponte (2013) estimated sub-footprint-scale salinity variability globally using a 1/12° solution from the Hybrid Coordinate Ocean Model (HYCOM): model salinities were binned into 1° × 1° grid boxes and the standard deviation of salinity taken as an estimate of the salinity sampling error, which is expected to be equivalent to the difference between a point measurement and a footprint-averaged measurement of SSS. Vinogradova and Ponte (2013) found the highest sampling errors of 1 psu were located in coastal regions with strong large-scale horizontal salinity gradients. Somewhat smaller sampling errors of 0.2 psu were found in regions with river outflow and boundary currents. Vinogradova and Ponte (2013) also found that in some places the sampling error due to small-scale salinity could be large enough to affect Aquarius validation.

3. Data and methods

a. *Thermosalinograph data*

This study is based on historical TSG data from the databases listed in Table 1. Only data for which the data providers have applied at least minimal quality control (QC), for example, removing data outside climatological ranges, were used. For data not designated "research quality," we applied further QC according to the procedure described below. The largest source of data was version 4 of the Surface Ocean CO_2 Atlas (SOCAT) database (Bakker et al. 2016; https://www.socat.info), which contains TSG measurements along with the CO_2 measurements from research vessels. SOCAT temperature and salinity measurements are only minimally controlled such that they are reasonable for calculating surface water CO_2 flux, so they were subjected to full QC for the present analysis. SOCAT data were supplemented with data from three additional databases. First, delayed-mode data from the French Sea Surface Salinity Observation Service (SSS-OS) have undergone a thorough QC procedure that includes comparison to bottle measurements, available float data, and climatology (Alory et al. 2015; http://www.legos.obs-mip.fr). However, temperature measurements from SSS-OS have only been checked with an automated processing code (Alory et al. 2015). Second, the Shipboard Automated Meteorological and Oceanographic System (SAMOS; http://samos.coaps.fsu.edu) provides TSG and meteorological data collected on research vessels and a select number of voluntary observing ships. Only SAMOS data with either "intermediate" or research-quality processing were used here; for the latter, no additional QC was performed. Third, the Global Ocean Surface Underway Data (GOSUD) project (www.gosud.org) is an international initiative to assemble in situ near-surface ocean

TABLE 1. Databases of TSG measurements used for the present study.

Data provider	No. of ships	No. of data points after QC	Date range	Reference
SOCAT	112	6.6×10^6	1990–2015	Bakker et al. (2016)
SSS-OS	29	4.9×10^6	1996–2016	Alory et al. (2015)
SAMOS	33	2.8×10^6	2006–17	Smith et al. (2009)
GOSUD	40	3.3×10^6	1997–2016	Gaillard et al. (2015)
JAMSTEC	1	2.3×10^6	1998–2016	JAMSTEC (2016)
M/V *Oleander*	1	2.0×10^6	2001–14	Rossby (2001)
AODN	4	1.2×10^6	2002–16	—
PANGAEA	2	5.3×10^5	1991–2016	Fahrbach et al. (2007)

temperature and salinity observations. GOSUD provides delayed-mode TSG data from research vessels and sailing ships. Data from several additional research vessels were obtained from the Japan Agency for Marine-Earth Science and Technology (JAMSTEC; R/V *Mirai*; http://www.godac.jamstec.go.jp/darwin/); PANGAEA data publisher (R/V *Polarstern*; https://www.pangaea.de/); and the Australian Ocean Data Network (AODN; R/V *Astrolabe*, R/V *Southern Surveyor*, R/V *Aurora Australis*, R/V *Tangaroa*, R/V *Cape Ferguson*, and R/V *Solander*; https://portal.aodn.org.au/). Finally, TSG measurements in the North Atlantic made from the container ship M/V *Oleander* were acquired from Stony Brook University (http://po.msrc.sunysb.edu/Oleander/).

We applied the additional QC procedures described in "TSG Data Quality Control" published by the National Oceanic and Atmospheric Administration's Atlantic Oceanographic and Meteorological Laboratory (NOAA/AOML; http://www.aoml.noaa.gov/phod/tsg/data/qc.php) to each dataset. Specifically, large data spikes and gradients and repeated occurrences of one value (i.e., stuck values) were flagged; then the data were visually inspected for any outliers and abnormalities (e.g., large spikes or unrealistic values that were not captured by the automated algorithms). Further QC removed data within 50 km of land, data points with salinity values outside the range of 0–40 psu or temperature values outside the range from −2° to 35°C, and measurements made when the ship was moving slower than $2\,\mathrm{m\,s^{-1}}$ or faster than $10\,\mathrm{m\,s^{-1}}$. Data with dates or locations that were physically impossible were also discarded.

Following the initial QC, the TSG data were compared to climatological temperature and salinity based on the Roemmich and Gilson (2009) Argo product, a $1° \times 1°$, monthly gridded product available from 2004 to present. The gridded values were linearly interpolated to the ship times and locations (with ship measurements before 2004 compared to the climatological average at their locations). TSG measurements were also compared to 5-m data from individual Argo floats that were found within 0.5° and 2 days of the TSG measurements. TSG data were often in better agreement with Argo float profile data than with the gridded Argo data, which are smoothed in time and space and therefore can miss transient values in space or time that are captured by the TSG and individual Argo profile data. This necessitated a two-stage QC procedure when using the Argo data to validate the TSG dataset. The first stage was to flag all TSG data points for which either salinity or temperature deviated more than ±2.5 psu or ±10°C, respectively, from either the gridded Argo data or the Argo profile data. The second stage removed the flags from TSG data points in cases where the salinity measurement was within 0.5 psu and the temperature measurement was within 2°C of the Argo profile values.

Depending on the amount of prior quality control, approximately 20%–50% of the raw measurements in each dataset were removed during the quality control procedure. Once the final quality control was completed, the different TSG datasets were merged. As there is some overlap between the TSG databases, care was taken to exclude data duplicated across multiple databases. Geographical and temporal data densities of the 2.4×10^7 individual TSG measurements resulting from the QC procedures are shown in Fig. 1. The spatial distribution of TSG measurements is shown in Fig. 1a: measurement density is high in shipping lanes (e.g., the North Pacific and North Atlantic Oceans), where a data density of more than 5000 measurements per $3° \times 3°$ grid box is common. The northern Indian Ocean is reasonably well covered, though with a more moderate data density of approximately 2000 measurements per grid box. The Southern Hemisphere basins have relatively sparse coverage, particularly the Indian Ocean. A histogram showing the distribution of TSG data as a function of time in Fig. 1b shows the majority of data were collected after 2005. The quality-controlled TSG data used in this work are publicly available at https://github.com/kdrushka/tsg-data/.

The response of conductivity sensors used in most TSGs is known to drift over time scales of weeks to months (Alory et al. 2015). This drift will lead to long-term changes in the reported salinity values. However,

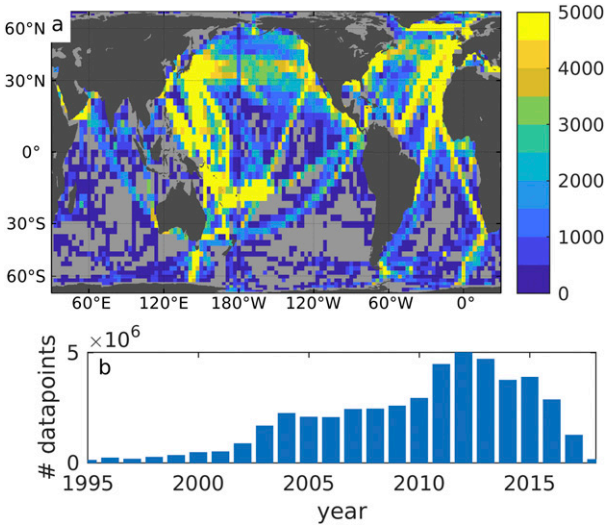

FIG. 1. Number of quality-controlled TSG data: (a) in each 3° × 3° grid box and (b) per year. Grid boxes with fewer than 100 data points are masked out in gray.

because this study is concerned with horizontal salinity variations on scales less than 100 km (covered in a few days, at most, by ships moving at ~5 m s^{-1}), long-term drift in conductivity sensors is not a concern and was ignored for this study. In addition, because the TSG is located in the ship's engine room, temperature measurements collected with shipboard TSGs often have a warm bias of order 0.1°C that varies with the configuration of the TSG system on a given ship (Delcroix and McPhaden 2002; Maes et al. 2013; Alory et al. 2015). This bias was assumed to be unimportant for characterizing variability on relatively small scales, and was ignored. It should be noted that the depth of the TSG water intake ranges between ships (typically between 5 and 10 m; Alory et al. 2015). Since the upper ~10 m of the ocean are typically well mixed, we assume that differences in TSG intake depth do not significantly affect the estimates of horizontal variability, and that the TSG salinity measurements provide a reasonable estimate of the ~1-cm depth salinity measured by L-band radiometers. An exception is low-wind, rainy regions where precipitation can produce strong vertical salinity gradients in the upper meters of the ocean (Asher et al. 2014a; Drushka et al. 2016); the implications of this are discussed further below. Near-surface vertical salinity gradients might also be present in regions where ice melt is a significant factor in upper-ocean salinity variability, but this has not been measured in the field.

b. *Characterizing submesoscale variability*

Submesoscale variability was estimated as fluctuations on lateral scales smaller than 20 km. Each individual ship transect was divided into nonoverlapping segments, each 20 km in length. A segment was rejected if the average spacing of measurements within the segment was greater than 2.5 km, if the ship took longer than 3 h to complete the segment, or if more than one of the data points in the segment were missing or flagged as suspect by the QC procedure. Globally, this resulted in a dataset consisting of over 830 000 20-km segments. Over the entire dataset, the number of points per 20-km segment was not constant due to differences in ship speed and sampling rate between ships. To avoid biases in estimating variability resulting from segments having different numbers of data points, salinity S and temperature T measurements within each segment were interpolated to have 2.5-km spacing, providing 9 data points per 20-km segment, including the endpoints. Because segments with data spaced farther apart than 2.5 km were rejected, interpolation did not generate unrealistic small-scale variability. Density ρ was computed for each pair of interpolated T and S.

For each segment, the mean of temperature, salinity, and density (T_{seg}, S_{seg}, and ρ_{seg}) as well as the position (x_{seg}, y_{seg}) of the ship and the time (t_{seg}) at the segment midpoint were computed. To quantify submesoscale variability, the standard deviation of temperature, salinity, and density were computed from the interpolated data within each segment, giving $\sigma_{T_{\text{seg}}}$, $\sigma_{S_{\text{seg}}}$, and $\sigma_{\rho_{\text{seg}}}$. Finally, these means and standard deviations were binned into 3° × 3° grid boxes. Grid boxes containing fewer than 10 ship-track segments were rejected. The median values of the $\sigma_{T_{\text{seg}}}$, $\sigma_{S_{\text{seg}}}$, and $\sigma_{\rho_{\text{seg}}}$ values within each grid box were then computed, giving $\sigma_S(x, y)$, $\sigma_T(x, y)$, and $\sigma_\rho(x, y)$, where x and y refer to the center of a grid box.

To estimate the contribution of sub-footprint-scale salinity variability to satellite uncertainties, the analysis of salinity measurements was repeated for segments 100 km in length (for a total of 160 000 segments, with 41 points per segment). In this case, the 95th percentile (rather than the median) of the $\sigma_{S_{\text{seg}}}$ values within each grid box were computed in order to estimate an upper limit on the variability in salinity.

c. *Density variability and compensation*

The compensation of density fronts is typically characterized using the density ratio R:

$$R = \frac{\alpha \Delta T}{\beta \Delta S}, \tag{1}$$

where ΔT and ΔS are the salinity difference over some horizontal distance Δx, and α and β are the thermal expansion and haline contraction coefficients of seawater,

respectively. When $R = 1$, temperature and salinity have equal and opposite effects on density, so there is no density difference over Δx, that is, the front is compensated (Rudnick and Ferrari 1999). Fronts for which R is positive are at least partially compensated, with $R > 1$ indicating that temperature has a stronger impact on density than salinity and $0 < R < 1$ indicating that salinity dominates. Fronts with $R < 0$ are anticompensated: salinity and temperature act constructively to create differences in density. These situations have the potential to produce strong density fronts; however, horizontal density gradients can slump due to gravity and may not persist (Rudnick and Ferrari 1999).

Because R tends toward infinity as ΔS approaches zero, the Turner angle (Tu) is often used in place of the density ratio to characterize front compensation:

$$\mathrm{Tu} = \arctan(R), \tag{2}$$

where Tu can be in the range from $-\pi/2$ to $+\pi/2$. $\mathrm{Tu} > 0$ implies density compensation is present since R must be positive definite, with $\mathrm{Tu} = \pi/4$ indicating a fully compensated front having $R = 1$. $\mathrm{Tu} < 0$ indicates anticompensation, meaning that changes in temperature and salinity are working together to create a density gradient. When $\mathrm{Tu} = 0$, changes in salinity are causing any observed density gradient whereas when $|\mathrm{Tu}| = \pi/2$ changes in temperature alone are driving density differences. Here, we compute the Turner angle over 10-km horizontal distances, chosen because this is typical of the mixed layer Rossby deformation radius at most latitudes, and hence compensation is expected to be most common at this scale or smaller (Rudnick and Martin 2002).

In this study, we estimate the prevalence of surface front compensation globally. We also introduce the density variability ratio R_ρ, an analog to the density ratio that quantifies the relative contributions of temperature and salinity variability (rather than the contributions of well-defined fronts) to density variability:

$$R_\rho = \frac{\alpha\sigma_T}{\beta\sigma_S}, \tag{3}$$

where σ_T and σ_S are the standard deviations of temperature and salinity, respectively, as described above. Because both σ_T and σ_S are greater than or equal to zero, the values for R_ρ can range from zero to approaching infinity, so it is also helpful to convert R_ρ into an angle, denoted θ_ρ, using

$$\theta_\rho = \arctan(R_\rho), \tag{4}$$

where θ_ρ lies within the range from 0 to $\pi/2$. A value of $\theta_\rho > \pi/4$ (i.e., $R_\rho > 1$) indicates that temperature variance is more important than salinity variance in generating density variability, and $\theta_\rho < \pi/4$ indicates that salinity variability dominates variability in density.

d. Satellite comparisons to Argo salinity

Individual Level 2 (not gridded) Aquarius, SMOS, and SMAP satellite salinity measurements were compared to Argo data. For this analysis, we used Aquarius version 5.0 data (NASA Aquarius Project 2017), which were obtained from NASA's Physical Oceanography Distributed Active Archive Center (PO.DAAC). The footprints for the three Aquarius radiometers are ellipsoidal and have the following dimensions: 76 km (along track) × 94 km (cross track), 84 km × 120 km, and 96 km × 156 km. Each of the beams was considered separately. Quality flags were applied to the Aquarius data following the Aquarius User Guide, with the additional step of flagging data that were moderately or severely contaminated by radio frequency interference (RFI). Aquarius data are available from August 2011 to June 2015. For this version of the Aquarius product, each salinity measurement is accompanied by an associated estimate of both random and systematic uncertainty (Meissner et al. 2018). The estimated systematic uncertainties are dominated by the effects of undetected RFI as well as uncertainties in the SST and wind speed used for the Aquarius corrections. Estimated random uncertainties are considered to have short time and space scales, and thus average out to some degree for monthly products; they are dominated by the effects of radiometer noise and wind speed. All uncertainties are enhanced at colder SSTs, where the sensitivity of the radiometer to salinity is lower (Meissner et al. 2018). Although the V5.0 Aquarius data product includes Argo surface salinity measurements that are collocated with the satellite footprints, in order to ensure consistency in how the Argo and Aquarius data were collocated, we performed our own collocation (described below). For all satellite products, data within 100 km of the coast were masked out and only data between 60°S and 60°N were considered.

The SMAP Level 2B Combined Active Passive (CAP) Sea Surface Salinity V4.0 Validated Dataset, produced by the NASA Jet Propulsion Laboratory (Fore et al. 2016), was also compared to Argo. The SMAP radiometer has an elliptical footprint of 38 km × 49 km, which is scanned conically over a circular swath with a diameter of approximately 1000 km. It should be noted that although the word "active" in CAP implies the use of radar measurements to correct for surface

TABLE 2. Statistics for Argo–satellite matchups and satellite uncertainties. Mean RMS difference is computed as the global mean average of the bin-averaged RMS differences between Argo and satellite salinities shown in Figs. 9a, 10a, and 11a. The "equal area" values of RMS difference in parentheses were computed only for the grid boxes in which all three satellites have data. Mean satellite uncertainties were computed for all satellite measurements (i.e., not only the matchup data). All statistics were computed for data between 60°S and 60°N.

Satellite	Date range	Search radius	No. of matchups	Mean RMS difference (equal area) (psu)	Mean satellite uncertainty (psu)
Aquarius	Aug 2011–Jun 2015	50 km	45 000	0.28 (0.28)	0.33
SMAP	Apr 2015–Dec 2017	25 km	69 000	0.83 (0.75)	0.93
SMOS	Jan 2011–Dec 2016	25 km	140 000	0.57 (0.51)	0.88

roughness in the data product, in fact the radar aboard SMAP failed soon after launch (in July 2015) so the SMAP CAP algorithm does not include an active term in the cost function (Tang et al. 2017). The algorithm used in the CAP product retrieves salinity from brightness temperatures by correcting for roughness estimated using wind speed from NOAA's Global Data Assimilation System (Fore et al. 2016). SMAP data from April 2015 to December 2017 were obtained from the PO.DAAC. The SMAP salinity data and associated uncertainty estimates were only used if their quality flag (bit 0) defined them as "usable data."

Finally, we made comparisons between Argo and the SMOS L2Q Level-2 Ocean Salinity product (CATDS 2017). The SMOS radiometer uses a synthetic array antenna, resulting in elliptical footprints whose dimensions are a function of look angle. The average footprint size is ~43 km (Kerr et al. 2010), which is comparable to the 40-km footprint size of SMAP observations (Meissner et al. 2017). Only measurements within ±300 km of the center of the swath were used. Data were used if they were classified as having valid salinities (flag class 1) and were rejected if they were classified as being outliers (flag class 28) by the SMOS algorithm. The SMOS L2Q product includes an uncertainty estimate for each salinity measurement. Long-term systematic errors have been removed from the product, so this uncertainty primarily represents random error (Boutin et al. 2018).

All delayed-mode Argo data from the relevant satellite time periods were obtained from the Argo repository at Institut Français de Recherche pour l'Exploitation de la Mer (IFREMER; Argo 2019). The shallowest salinity measurement from each profile was used; if the shallowest depth was deeper than 5 m, data from that profile were discarded. Argo data were matched to each of the three satellite products by identifying satellite measurements made within a search radius approximating the satellite footprints and within ±1 day of a given Argo measurement. The size of the search radius and number of matchups for each satellite product are shown in Table 2.

Satellite–Argo salinity differences were estimated by sorting the matched Argo–satellite pairs into 5° × 5° grid boxes: the bias (mean difference between the Argo and satellite salinities) in each grid box was removed, then the root-mean-square (RMS) difference between the Argo and debiased satellite salinity measurement was computed (Table 2). By removing the bias, we isolated differences that are due to random noise or spatial mismatches between the Argo and satellite data. Grid boxes with fewer than 15 Argo–satellite pairs were masked out.

The uncertainty estimates provided with each satellite product were also binned into 5° × 5° grid boxes. The RMS of the individual uncertainty estimates was used to estimate to be the mean uncertainty for each grid box. The global-mean uncertainty was then estimated as the average of the gridded uncertainties.

4. Results

a. Global patterns of submesoscale surface variability

Examples of TSG measurements made in four different regions are shown in Fig. 2. Each example is representative of observations from that region. South of Tasmania in the Southern Ocean, fronts tend to be compensated: temperature and salinity vary together, and the resulting density variability is weak (Fig. 2a). In the southern Indian Ocean west of Australia, fronts tend to be strongly anticompensated, with temperature and salinity anomalies contributing constructively to form strong density gradients (Fig. 2b). In the Amazon plume region, fronts can be weakly anticompensated, with salinity contributing more to density variability than temperature, resulting in moderately strong density variability that resembles salinity (Fig. 2c). Finally, in the southwest Pacific southeast of Australia, salinity variability is weak, and temperature dominates the strong density variability (Fig. 2d). These examples demonstrate that density fronts are controlled by the strength of the temperature and/or salinity gradients, and by the degree of compensation

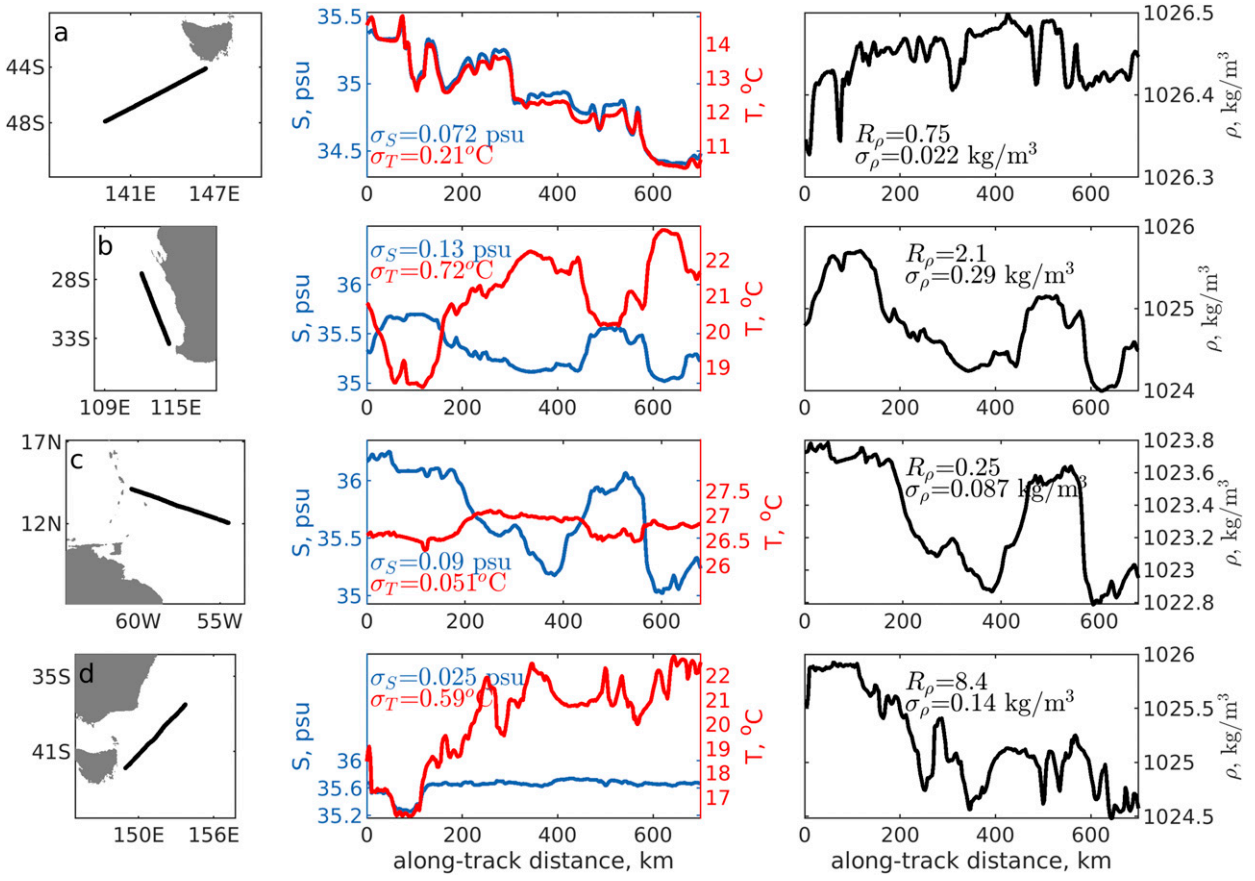

FIG. 2. Examples of TSG data in four regions: (a) southwest of Tasmania (data from 1–2 Jan 2015) showing compensated density fronts; (b) west of Australia (13–14 Jul 2014) showing anticompensated density fronts; (c) the Amazon plume (14–15 Mar 2004) showing that salinity dominates the density variability; and (d) southeast of Australia (10–11 Feb 2015) showing that temperature dominates the density variability. (left) A map with one example ship track. (center) Salinity and temperature along that track: for each example, the y axes for both salinity and temperature have been scaled with the local α and β such that both represent the same density range. Values of α and β for each example are as follows: $\alpha = 1.9 \times 10^{-4}\,(°C)^{-1}$, $\beta = 7.5 \times 10^{-4}\,\text{psu}^{-1}$ in (a); $\alpha = 2.7 \times 10^{-4}\,(°C)^{-1}$, $\beta = 7.3 \times 10^{-4}\,\text{psu}^{-1}$ in (b); $\alpha = 3.1 \times 10^{-4}\,(°C)^{-1}$, $\beta = 7.2 \times 10^{-4}\,\text{psu}^{-1}$ in (c); and $\alpha = 2.6 \times 10^{-4}\,(°C)^{-1}$, $\beta = 7.3 \times 10^{-4}\,\text{psu}^{-1}$ in (d). (right) Density. Values of median σ_S, σ_T, σ_ρ, and R_ρ over 20-km scales for each transect are displayed.

between temperature and salinity. The local values of the haline contraction and thermal expansion coefficients also help determine the relative impacts of temperature and salinity on density [Eqs. (1) and (3)]. At higher latitudes, α is relatively small and β relatively large (see Fig. 3). However, this does not imply that salinity necessarily dominates density variability at high latitudes, nor that temperature dominates at low latitudes. For instance, in the Amazon plume region (Fig. 2c), salinity variability dominates density ($R_\rho < 1$) even though α is relatively large there (Fig. 3). In contrast, south of Tasmania, β is relatively large and thus salinity variability dominates density ($R_\rho < 1$) despite the strong temperature variability (Fig. 2a).

Figure 4 shows the global distribution of submesoscale salinity, temperature, and density, and Fig. 5 shows the mean surface salinity, temperature, and density, where all properties are calculated from the TSG dataset as described above. Comparing Fig. 4 with Fig. 5 does not reveal any obvious correlation between the magnitude of a mean surface property and the magnitude of its corresponding variance. However, commonalities between the processes that govern variance are seen when looking at the data on a region-by-region basis.

Figure 4a shows that regions influenced by river outflows have strong submesoscale salinity variability, with $\sigma_S > 0.05$ psu seen in the western equatorial Atlantic Ocean (Amazon River), southwestern Atlantic (Rio Plata), northern Bay of Bengal (Ganges–Brahmaputra River), Gulf of Guinea (Congo and Niger Rivers), and Gulf of Mexico (Mississippi River). Submesoscale salinity variability is also strong ($\sigma_S > 0.05$ psu) in the Gulf Stream, where the large-scale fronts generate submesoscale variance. Additionally, large-scale salinity gradients

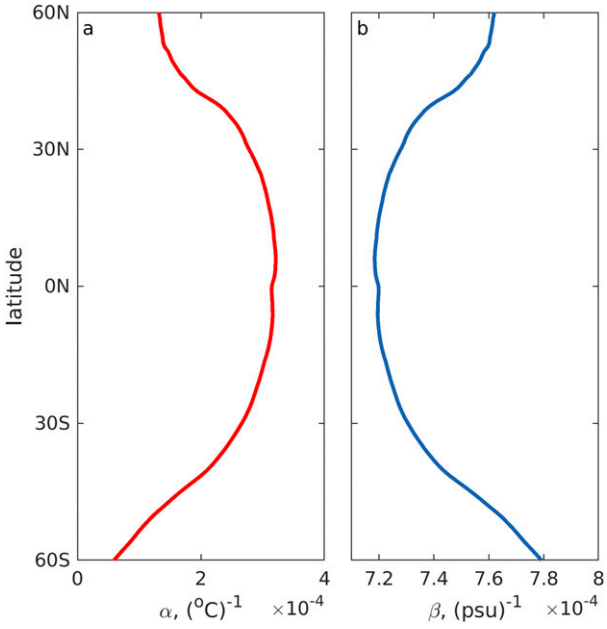

FIG. 3. Longitudinally averaged (a) thermal expansion coefficient and (b) haline contraction coefficient.

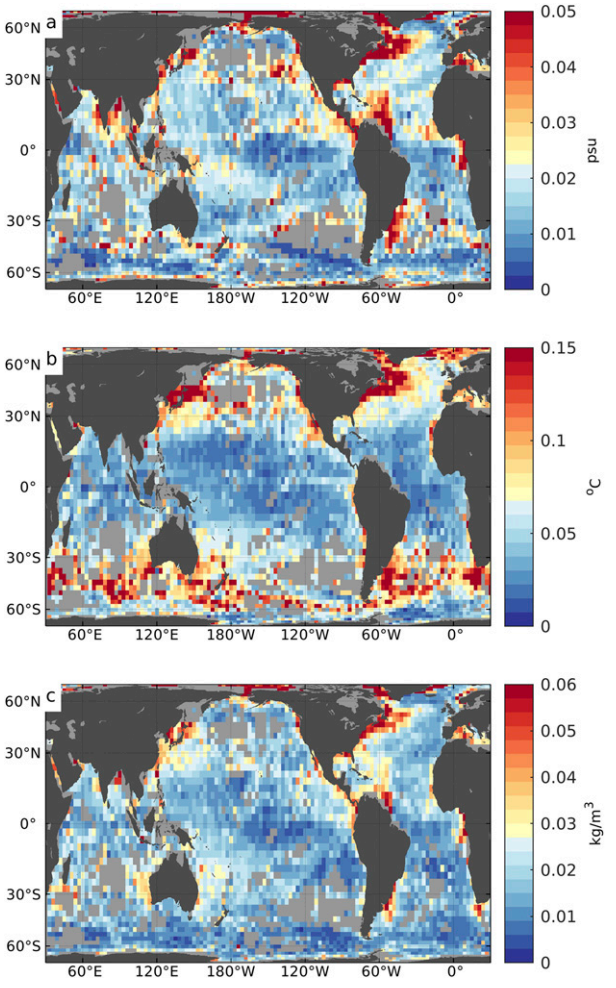

FIG. 4. Variability of submesoscale sea surface (a) salinity, (b) temperature, and (c) density, computed as the standard deviation along 20-km ship transects. Regions with insufficient TSG data are masked out.

appear to generate submesoscale variability in a narrow (<5°) zonal band that varies in latitude between 30° and 50°S in all basins, and in the North Pacific between 30° and 50°N. These zonal bands both correspond to relatively strong meridional gradients in mean salinity (Fig. 5a), suggesting the importance of instabilities at, or displacements of, large-scale fronts in generating submesoscale salinity variability (e.g., Kolodziejczyk et al. 2015). Ocean regions that are influenced by ice melt, such as waters east and west of Greenland and the North Sea west of Scandinavia, also have strong salinity variability. Consistent with results from recent field experiments (e.g., Bosse et al. 2015), submesoscale salinity variability is found to be strong in the western Mediterranean Sea. Finally, submesoscale salinity variability is moderately enhanced ($\sigma_S \sim 0.025$ psu) in the tropics, from the western Pacific through the central tropical Atlantic. These are the tropical rain belts, where the horizontal (and vertical) variability of salinity is large due to the ''lenses'' of buoyant fresher water that sit on the ocean surface for a number of hours after it rains (e.g., Asher et al. 2014a; Drushka et al. 2016). It is possible that σ_S is underestimated in these areas since these rain-generated fresh layers are typically $O(1)$ m deep, with a typical surface salinity anomaly of up to several psu that decays rapidly with depth (Drushka et al. 2016). As a result, in these regions ships' TSGs sampling at 5–10-m depth in these regions likely capture relatively weaker salinity variance compared to the salinity variability at the surface. It is also likely that some mixing occurs due to flow around the ship, reducing the small-scale gradients; this effect cannot be estimated from the TSG dataset, but it is expected to be small.

Although evaporation produces surface salinity anomalies, it is not expected that evaporation will produce significant submesoscale salinity variability over the depths sampled by TSGs. First, evaporation only produces weak salinity anomalies at the sea surface (Asher et al. 2014b); when mixed to the 5–10-m depth of the TSG measurements, the salinity anomaly would be undetectable. Second, conditions leading to evaporative near-surface salinity anomalies (high downwelling shortwave radiation coupled with low wind speed) tend to be similar over broad spatial scales and hence will not produce small-scale variability. In contrast, freshwater forcing from rain or rivers tends to be relatively localized and hence can generate horizontal variance on small scales.

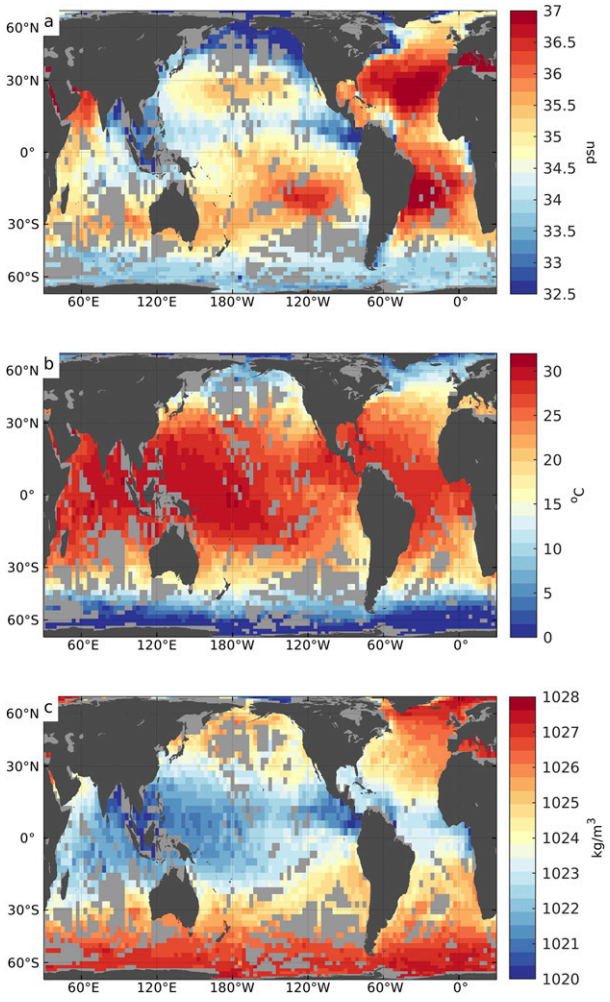

FIG. 5. Mean sea surface (a) salinity, (b) temperature, and (c) density from TSG measurements.

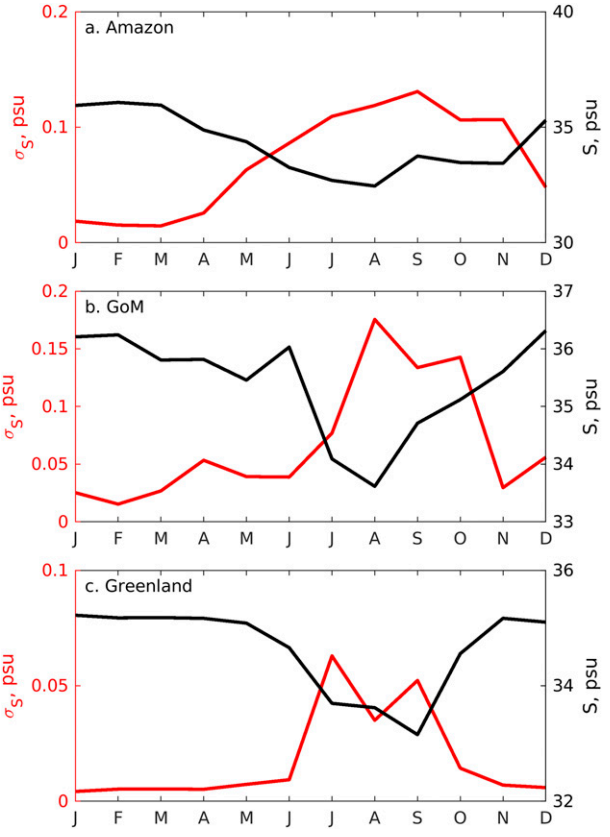

FIG. 6. Monthly estimates of σ_S (red) and mean salinity (black): (a) in the Amazon outflow region (4°–16°N, 60°–35°W); (b) in the northern Gulf of Mexico (21°–30°N, 100°–85°W); and (c) east of Greenland (55°–69°N, 58°–38°W).

Submesoscale salinity variability is low ($\sigma_S < 0.02$ psu) throughout much of the open ocean, in particular far away from coastal boundaries, river plumes, regions affected by ice melt, and strong currents where instability generates submesoscale variability.

In regions for which seasonal phenomena (ice melt, river runoff, monsoon rainfall) generate the horizontal salinity variance, salinity variance is also expected to vary seasonally. Although the data coverage is not adequate to explore this in detail over the entire globe, several examples from specific regions are shown in Fig. 6. Maximum river outflow results in lower salinity (noting that there can be a delay between maximum outflow and minimum SSS): this is seen during May–November in the Amazon plume region (Fig. 6a) and during July–September in the Gulf of Mexico (Fig. 6b). An increase in river outflow leads to enhanced fronts and filaments, and hence an increase in submesoscale salinity variability, as can be seen from the corresponding increases in σ_S in both plume regions. Similarly, the sea surface east of Greenland is freshest in July–September, when ice is melt is strongest, and this summertime freshening also correlates with a sharp enhancement in submesoscale salinity variability (Fig. 6c).

Submesoscale temperature variability σ_T is strongest ($\sigma_T > 0.15$°C) in major currents (e.g., Kuroshio, Gulf Stream, Agulhas), and in the Arctic Ocean (see Fig. 4b). The large mean meridional temperature gradient from 30° to 50°S (Fig. 5b) also results in strong submesoscale temperature variability throughout that zonal band. Eastern boundary regions such as the California, Canary, and Peru–Chile Currents display strong temperature variability near the coast, where upwelling of cold water drives strong temperature gradients and hence submesoscale features (e.g., Capet et al. 2008). In many cases, regions with high σ_S are coincident with high σ_T regions: for example, the Gulf Stream, the North Atlantic east and west of Greenland, and the Agulhas Current. However, there are also regions with high σ_S but low σ_T, primarily in areas influenced by river

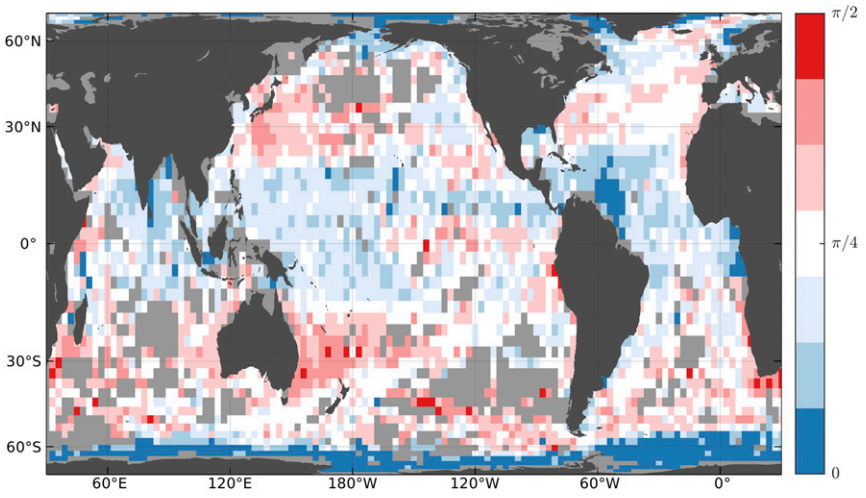

FIG. 7. Density ratio angle θ_ρ [Eq. (4)] computed from the standard deviation of temperature and salinity over 20-km segments of ship track.

plumes (e.g., Amazon plume, Bay of Bengal, Gulf of Guinea) or strong tropical rains (intertropical convergence zones and South Pacific convergence zone). Conversely, the 30°–50°S region in the Southern Ocean has high σ_T but generally low σ_S apart from the thin band described above.

Figure 4c shows the global pattern of submesoscale surface density variability σ_ρ and Fig. 5c shows the global pattern of mean density. Unsurprisingly, submesoscale density variability is strongest ($\sigma_\rho > 0.06\,\mathrm{kg\,m^{-3}}$) in regions with large σ_S and/or σ_T: western boundary currents, river plumes, eastern boundary upwelling regions, and regions influenced by ice melt (see Fig. 4c). The density variability ratio [Eq. (4)] is a simple metric for diagnosing where salinity versus temperature drives submesoscale density variability (Fig. 7). Salinity variability drives submesoscale density variability ($\theta_\rho < \pi/4$) at high latitudes (where β is much greater than α; see Fig. 3) and in regions with high freshwater input, such as occur in the tropics or in river plumes. Temperature dominates submesoscale density variability ($\theta_\rho > \pi/4$) over subtropical and subpolar latitudes, where the large-scale meridional temperature gradient is strong (Fig. 5b) so that σ_T is also large (Fig. 4b).

Although Fig. 7 describes the relative importance of salinity and temperature in generating σ_ρ, it does not show whether salinity and temperature fronts tend to have opposing effects on density (i.e., density-compensated fronts) or if they act together to produce strong density fronts (i.e., anticompensated fronts, which are expected to slump). Figure 8 shows a global map of the Turner angle [Tu; Eq. (2)] computed over 10 km lateral distances with regions containing compensated fronts (Tu > 0) shaded in pale colors and regions with noncompensated fronts (Tu < 0) shaded in darker tones. Regions containing fronts for which salinity dominates are blue (Tu near zero), and those for which temperature dominates are red or pink (Tu near $\pm\pi/2$). Unsurprisingly, Fig. 8 tells a similar story to Fig. 7 in terms of where submesoscale density fronts are dominated by salinity (generally, in the high latitudes and tropics) versus temperature (midlatitudes and subpolar latitudes). Figure 8 additionally demonstrates that fronts on 10-km lateral scales tend to be at least somewhat compensated globally, consistent with previous findings (Rudnick and Martin 2002). The exception is in the south Indian and southwest Pacific Oceans between 15° and 30°S, where anticompensation dominated by temperature fronts (red colors) is seen. In these regions, temperature variability is moderate ($\sigma_T \sim 0.08$°C; Fig. 4b), and salinity variability, though weak (Fig. 4a), contributes constructively to density, so the resulting σ_ρ is moderately strong ($\sim 0.03\,\mathrm{kg\,m^{-3}}$; Fig. 4c). This is demonstrated by the example in Fig. 2b. Thin zonal bands of anticompensated fronts are also seen in each basin at the transitions between the salinity-dominated and temperature-dominated regions (e.g., around ~20°N in the Pacific, 5°–15°S in the Atlantic, and ~55°S in all basins; Fig. 8). This is consistent with the temperature-dominated, anticompensated fronts observed previously in the Pacific at 28°N (Hosegood et al. 2006). This analysis does not provide sufficient information to indicate whether density fronts tend to persist in these areas rather than slump and disperse horizontally, or if they are short-lived features that occur frequently and thus happen to be sampled often.

While there is a tendency to have compensated fronts (i.e., positive Turner angle) over much of the globe, there are few regions for which submesoscale temperature and

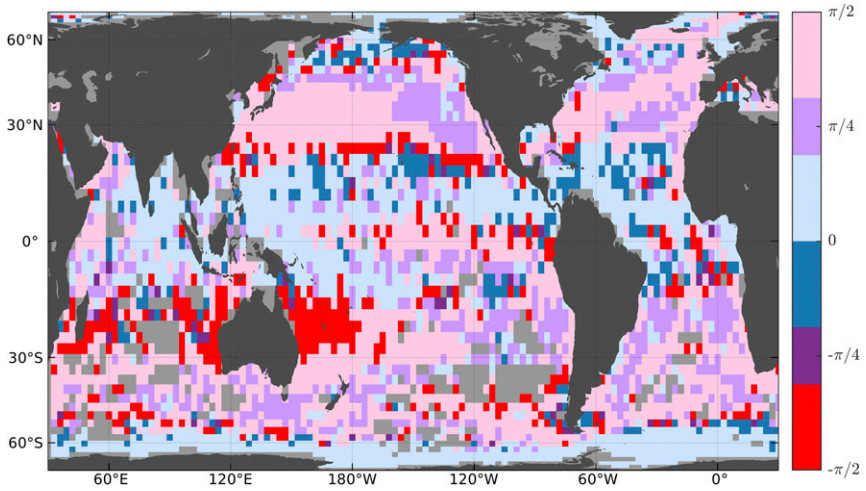

FIG. 8. Turner angle [Tu; Eq. (2)] computed over 10-km horizontal scales.

salinity are exactly compensated (Tu = $\pi/4$, pale purple in Fig. 8). As expected, these regions where fronts are fully compensated generally correspond to regions with small σ_ρ (Fig. 4c). For example, south of Australia, σ_S is relatively small (Fig. 4a), but β is large (Fig. 5a), so the contribution of salinity variability to density variability is large enough to compensate for the relatively strong temperature fronts (also seen in Fig. 2a). In the midlatitude North Pacific and North Atlantic east of the western boundary current extensions, fronts tend to be compensated, which explains why σ_ρ is relatively small despite moderate σ_S and σ_T values. Similarly, at the eastern edge of the South Atlantic Current, both temperature and salinity fronts are strong and compensated, leading to much weaker density fronts and low σ_ρ. In most other regions where fronts are compensated, temperature and salinity fronts are both weak, so density fronts are weak regardless of the compensation (e.g., the eastern Pacific and Atlantic between 15° and 30°S).

b. *Uncertainties in satellite salinity*

TSG measurements have been used to demonstrate that submesoscale salinity variability is a major driver of submesoscale density variability in a number of regions (Fig. 7). We now consider the impact of surface salinity variability on satellite salinity validation. The footprints of the salinity satellites range from ~40 to 100 km in diameter, so we compute σ_S within 100-km segments of data, taking the 95th percentile value of the estimates within each grid box in order to estimate the upper end of sub-footprint-scale salinity variability, as shown in Fig. 9a. A comparison of Fig. 4a and Fig. 9a shows that the broad patterns of horizontal salinity variability are the same whether computed over 20- or 100-km scales. Indeed, σ_S patterns are generally independent of the scale over which they are calculated (at least for scales smaller than a few hundred kilometers). This is because the phenomena generating the salinity variability (e.g., river plumes, ice melt, large-scale gradients) are larger than this scale. In addition, the standard deviations computed from individual ship tracks are binned into 3° × 3° grid boxes, obscuring differences between 20- and 100-km scales. (Note that the σ_S values computed over 100-km scales have larger amplitudes than those computed over 20-km scales. This is because there are 41 data points per 100-km segment and 9 per 20-km segment, including end points, and because the 95th percentile value is used for the 100-km segments compared to the median for 20-km segments).

Averaged globally, TSG-derived salinity variability (Fig. 9a) has a median value of 0.05 psu over 100-km scales, with 95% of the values smaller than 0.2 psu. These results are consistent with variability estimates produced by Vinogradova and Ponte (2013) using numerical data from the HYCOM model. Figure 9b shows mean salinity differences between Aquarius and collocated Argo measurements: globally, the root-mean-square difference between Aquarius and Argo salinity is 0.28 psu (Table 2). This is close to the global average of the uncertainty estimate of the Aquarius salinity product (sum of the systematic and random uncertainty estimates; Figs. 9c,d), which has a value of 0.33 psu (Table 2). The Aquarius–Argo differences generally resemble the systematic plus random uncertainty estimates on Aquarius data, as noted by Meissner et al. (2018). They are largest (0.5 psu) at latitudes higher than 40° in both hemispheres. This is primarily because the accuracy of the satellite salinity retrievals is worse at colder temperatures, which is reflected in both the random and systematic Aquarius uncertainties (Figs. 9c,d).

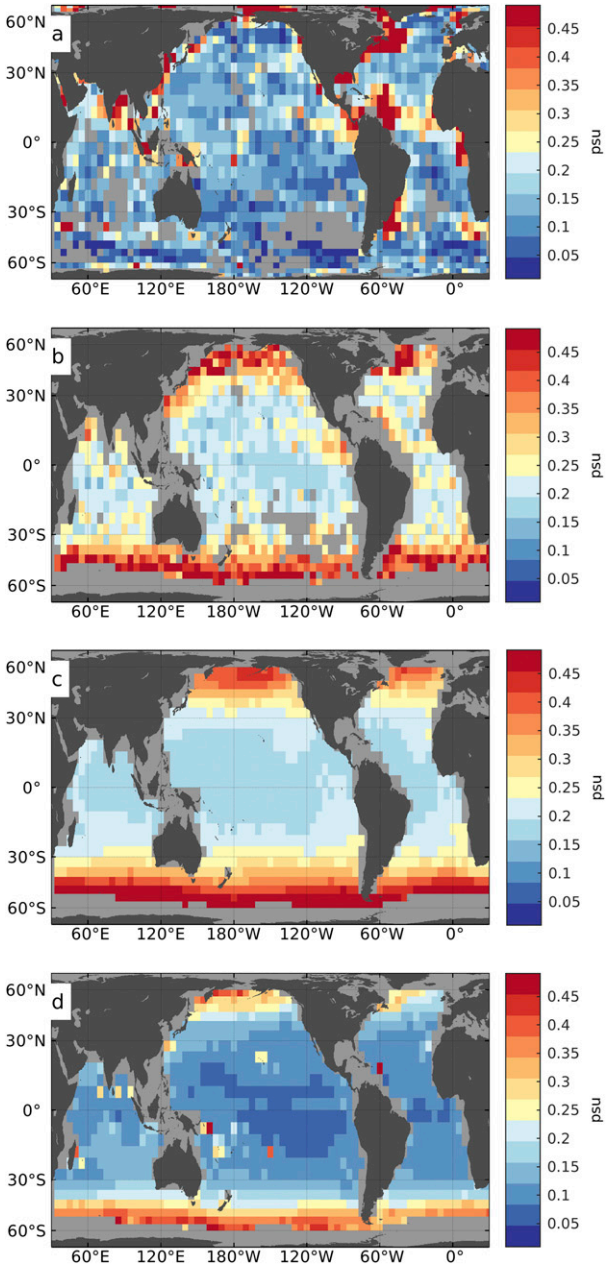

FIG. 9. (a) Variability of sea surface salinity on <100-km scales, computed as the standard deviation of SSS along 100-km ship transects. (b) Bin-averaged RMS difference between Argo surface salinities and Aquarius (v5 L2 data) salinities within ±50 km of the Argo floats. (c) Random and (d) systematic uncertainty on Aquarius salinity measurements from the Aquarius product.

The estimated random uncertainties are >0.4 psu at high latitudes and <0.2 psu equatorward of 40° (Fig. 9c). Systematic uncertainties are relatively low (<0.1 psu) throughout most of the ocean apart from high latitudes. In a number of regions, the Aquarius–Argo differences are relatively large (0.3 psu) but systematic and random uncertainties are low: for example, in the Bay of Bengal, Gulf Stream, Amazon plume, eastern equatorial Pacific, and equatorial Atlantic. These are all regions for which sub-footprint-scale salinity variability is strong (order 0.5 psu; Fig. 9a). Indeed, a comparison of the panels in Fig. 9 suggests that the Aquarius–Argo salinity differences that are not due to random or systematic uncertainties appear to arise from sub-footprint-scale salinity variability. This finding is significant because it implies that in regions with large σ_S, the large Aquarius–Argo differences do not represent errors in satellite retrieval of salinity; rather, they reflect the fact that Argo point measurements cannot represent spatially averaged satellite data when salinity is highly variable on scales smaller than one satellite pixel.

Figure 10a shows the mean salinity differences between SMAP and collocated Argo measurements. SMAP salinity measurements are much noisier than Aquarius measurements when compared to Argo, with a global-mean RMS difference of 0.83 psu (Table 2). Figure 10b shows that the estimated uncertainties of SMAP data (part of the SMAP data product), while larger than those for Aquarius (mean 0.93 psu; Table 2), cannot account for the SMAP-Argo differences, and there is no clear enhancement of SMAP–Argo differences in regions with strong small-scale salinity variability such as in river plumes (Fig. 9a). In other words, noise in the SMAP product appears to dominate the SMAP–Argo mismatches and hides the effect of sub-footprint-scale salinity variability that is seen in Aquarius data. Note that SMAP displays considerably better performance when compared with a monthly gridded Argo salinity product (Tang et al. 2017).

Figure 11a shows global SMOS–Argo RMS differences. Globally, the mean difference is 0.57 psu: larger than that of Aquarius but lower than that of SMAP (Table 2). Although earlier SMOS products had problems near coastlines, particularly in capturing fresh signals due to river plumes, the L2Q product used here has been shown to perform well in these regions (Boutin et al. 2018). The estimated uncertainties for the SMOS measurements are similar to those for SMAP, with a global mean of 0.88 psu (Fig. 11b; Table 2). However, unlike both SMAP and Aquarius, these estimated uncertainties are much larger than the mean satellite–Argo RMS differences. Outside of the high-latitude bands, where uncertainty due to cold SSTs is known to be large (Fig. 11b), SMOS–Argo differences are strongest in the same regions where σ_S is large: the Bay of Bengal, Panama Bight, Amazon plume, and the South Atlantic Current (see also Fig. 9a). Therefore, in accord with the Aquarius–Argo mismatches, the SMOS–Argo mismatches can be attributed, at least in part, to salinity

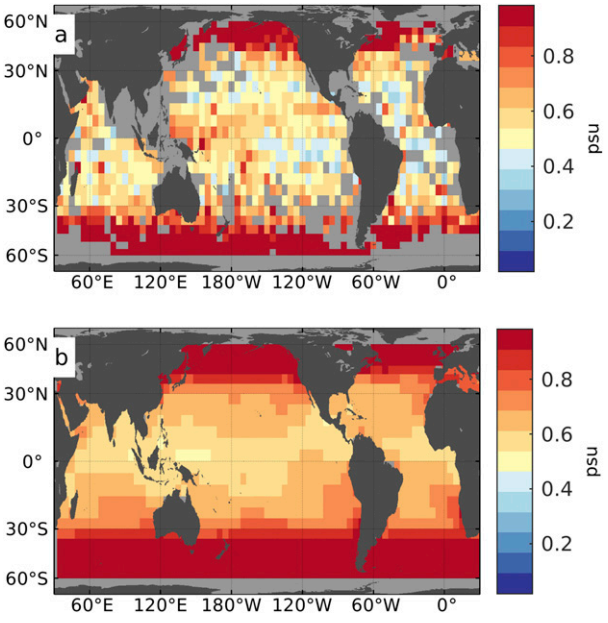

FIG. 10. (a) Bin-averaged RMS difference of salinity difference between Argo surface salinities and SMAP (v4 L2 data) salinities within ±25 km of the Argo floats. (b) Total (systematic plus random) uncertainty on SMAP salinity measurements from the SMAP product. Note that scaling is different than in Fig. 9.

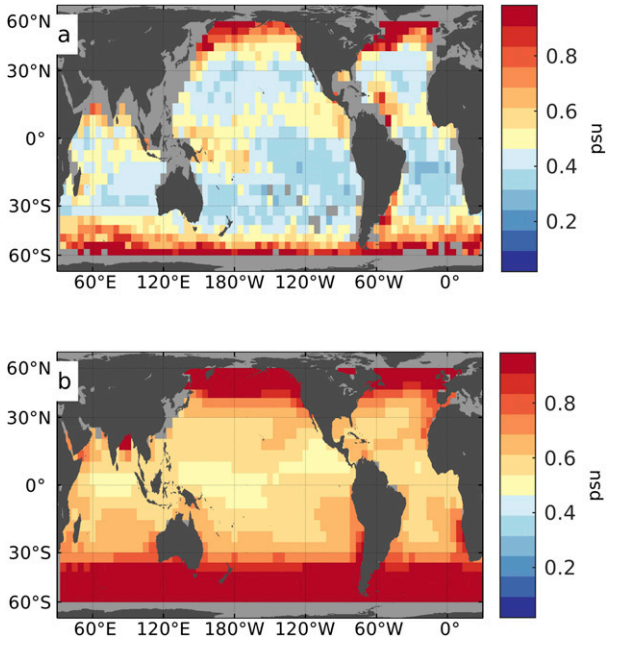

FIG. 11. (a) Bin-averaged RMS difference of salinity difference between Argo surface salinities and SMOS (L2Q data) salinities within ±25 km of the Argo floats. (b) Total uncertainty on SMOS salinity measurements from the SMOS product.

variability within SMOS pixels. In addition, contamination of SMOS salinity retrievals from RFI is problematic in certain regions (e.g., Bay of Bengal, Arabian Sea; Boutin et al. 2018), and likely accounts for some of the Argo–SMOS differences. In the intertropical convergence zone and South Pacific convergence zone, the SMOS–Argo differences are much more prominent than seen in Aquarius–Argo comparisons (Fig. 9b). This difference is likely because Aquarius is processed with different algorithms for rainy conditions; the SMOS L2Q processing algorithm does not flag fresh values in regions with high salinity variance such as the rainbands (Boutin et al. 2018). In addition, SMOS has a smaller spatial footprint than Aquarius, so the surface freshening from small tropical rain cells, which are typically O(1–10) km in horizontal scale, covers a greater fraction of a SMOS pixel and hence tends to cause a greater mismatch with Argo measurements made at depths of a few meters (e.g., Boutin et al. 2014).

5. Summary and discussion

More than 2.4×10^7 individual temperature and salinity measurements, combined from several databases of historical ship data, were combined to give a view of regional patterns of submesoscale variability of temperature, salinity, and density at the sea surface with unprecedented spatial resolution. We demonstrate the importance of salinity variability on scales smaller than 20 km for generating surface density variability. In river plumes (particularly the Amazon plume, in the Bay of Bengal, Gulf of Guinea, and Gulf of Mexico), east and west of Greenland, and in the Gulf Stream, South Atlantic, and Agulhas Currents, submesoscale surface salinity variability is large ($\sigma_S > 0.05$ psu over 20-km scales; Fig. 4a). Surface density variability σ_ρ also tends to be strong in these regions (Fig. 4c). Horizontal salinity variability appears to explain some of the discrepancies when Aquarius satellite salinity measurements are compared to in situ salinity measurements from Argo floats: specifically, outside of the high latitudes (where both random and systematic errors in Aquarius are large), the mismatch between Argo and Aquarius is largest in regions with large σ_S (Fig. 9). The SMOS–Argo differences in these same regions can also be explained to some extent by sub-footprint-scale salinity variability (Fig. 11a). In contrast, the SMAP salinity product is much noisier than either Aquarius or SMOS and it does not appear that sub-footprint-scale salinity variability has a significant effect on SMAP-Argo comparisons (Fig. 10).

Figure 7 highlights the important role of salinity variability in generating submesoscale surface density variability: throughout the tropical rainbands, river outflow regions, and in polar regions, density variability is dominated by salinity rather than temperature. In these regions, characterizing submesoscale

ocean dynamics requires an understanding of the salinity variability. This has been explored through several recent field campaigns, including the Air–Sea Interactions Regional Initiative experiment in the Bay of Bengal (MacKinnon et al. 2016), the ArcticMix experiment in the Arctic (MacKinnon et al. 2016), and the second Salinity Processes in the Upper Ocean Regional Study in the rainband of the tropical eastern Pacific Ocean (Lindstrom et al. 2019).

In regions where density variability is dominated by temperature, submesoscale temperature fronts (which can be tracked with high-resolution satellite SST maps; e.g., Cayula and Cornillon 1992; Belkin and O'Reilly 2009) likely explain much of the density variability. In contrast, submesoscale density fronts in salinity-dominated regions cannot be easily examined from satellite measurements, as the resolution of current satellite salinity products is too coarse (40–100 km) to capture the salinity variations that drive density.

On 10-km horizontal scales, fronts tend to be compensated to at least some degree throughout most of the global oceans, consistent with the suggestion of Rudnick and Martin (2002) that compensated fronts are ubiquitous because noncompensated fronts tend to slump and disperse horizontally. An exception is in the south Indian and southwest Pacific Oceans between 20° and 30°S, where fronts tend to be anticompensated, leading to relatively strong density variability. Fronts are not generally perfectly compensated (i.e., where temperature and salinity impacts on density cancel out exactly). The regions where both temperature and salinity variability are strongest—the Kuroshio, Gulf Stream, South Atlantic, and Agulhas Currents—tend to be compensated at their eastern edges, reducing the eastward extent of submesoscale density variability associated with these energetic currents.

Acknowledgments. We gratefully acknowledge the many groups who quality control, organize, and make available the TSG data used in this study (Table 1): SSS-OS, GOSUD, SAMOS, SOCAT, JAMSTEC, PANGAEA, AODN, and Stony Brook University. Aquarius L2 V5 data (http://dx.doi.org/10.5067/AQR50-2SOCS) were obtained from NASA's Physical Oceanography Distributed Active Archive Center (PO.DAAC). SMAP L2B V4 data are produced by the NASA Jet Propulsion Laboratory Climate Oceans and Solid Earth group (http://dx.doi.org/10.5067/SMP40-2TOCS) and were obtained from the PO.DAAC. The SMOS L2Q Ocean Salinity data were obtained from the "Centre Aval de Traitement des Données SMOS" (CATDS), operated for the "Centre National d'Etudes Spatiales" (CNES, France) by IFREMER (Brest, France). Argo profile data were collected and made freely available by the International Argo Program and the national programs that contribute to it (http://www.argo.ucsd.edu, http://argo.jcommops.org). The Argo Program is part of the Global Ocean Observing System. We acknowledge Sophie Clayton for valuable discussions; Jacqueline Boutin, Audrey Hasson, and Alexandre Supply for information about the SMOS data products; and Hsun-Ying Kao for discussion about Aquarius uncertainties. Finally, we thank two anonymous reviewers for their valuable feedback. This work was funded by NASA Grants NNX14AQ54G and NNX17AK04G.

REFERENCES

Alory, G., and Coauthors, 2015: The French contribution to the voluntary observing ships network of sea surface salinity. *Deep-Sea Res. I*, **105**, 1–18, https://doi.org/10.1016/j.dsr.2015.08.005.

Argo, 2019: Argo float data and metadata from Global Data Assembly Centre (Argo GDAC). SEANOE, accessed 1 January 2019, https://doi.org/10.17882/42182.

Asher, W. E., A. T. Jessup, R. Branch, and D. Clark, 2014a: Observations of rain-induced near surface salinity anomalies. *J. Geophys. Res. Oceans*, **119**, 5483–5500, https://doi.org/10.1002/2014JC009954.

——, ——, and D. Clark, 2014b: Stable near-surface ocean salinity stratifications due to evaporation observed during STRASSE. *J. Geophys. Res. Oceans*, **119**, 3219–3233, https://doi.org/10.1002/2014JC009808.

Backhaus, J. O., and J. Kämpf, 1999: Simulations of sub-mesoscale oceanic convection and ice–ocean interactions in the Greenland Sea. *Deep-Sea Res. II*, **46**, 1427–1455, https://doi.org/10.1016/S0967-0645(99)00029-6.

Bakker, D., and Coauthors, 2016: A multi-decade record of high quality fCO_2 data in version 3 of the Surface Ocean CO_2 Atlas (SOCAT). *Earth Syst. Sci. Data*, **8**, 383–413, https://doi.org/10.5194/essd-8-383-2016.

Belkin, I. M., and J. E. O'Reilly, 2009: An algorithm for oceanic front detection in chlorophyll and SST satellite imagery. *J. Mar. Syst.*, **78**, 319–326, https://doi.org/10.1016/j.jmarsys.2008.11.018.

Boccaletti, G., R. Ferrari, and B. Fox-Kemper, 2007: Mixed layer instabilities and restratification. *J. Phys. Oceanogr.*, **37**, 2228–2250, https://doi.org/10.1175/JPO3101.1.

Bosse, A., P. Testor, L. Mortier, L. Prieur, V. Taillandier, F. d'Ortenzio, and L. Coppola, 2015: Spreading of Levantine Intermediate Waters by submesoscale coherent vortices in the northwestern Mediterranean Sea as observed with gliders. *J. Geophys. Res. Oceans*, **120**, 1599–1622, https://doi.org/10.1002/2014JC010263.

Boutin, J., and Coauthors, 2016: Satellite and in situ salinity: Understanding near-surface stratification and sub-footprint variability. *Bull. Amer. Meteor. Soc.*, **97**, 1391–1407, https://doi.org/10.1175/BAMS-D-15-00032.1.

——, and Coauthors, 2018: New SMOS sea surface salinity with reduced systematic errors and improved variability. *Remote Sens. Environ.*, **214**, 115–134, https://doi.org/10.1016/j.rse.2018.05.022.

——, N. Martin, G. Reverdin, S. Morisset, X. Yin, L. Centurioni, and N. Reul, 2014: Sea surface salinity under rain cells: SMOS satellite and in situ drifters observations. *J. Geophys. Res. Oceans*, **119**, 5533–5545, https://doi.org/10.1002/2014JC010070.

Brando, V., and Coauthors, 2015: High-resolution satellite turbidity and sea surface temperature observations of river plume interactions during a significant flood event. *Ocean Sci.*, **11**, 909–920, https://doi.org/10.5194/os-11-909-2015.

Capet, X., J. C. McWilliams, M. J. Molemaker, and A. Shchepetkin, 2008: Mesoscale to submesoscale transition in the California Current System. Part I: Flow structure, eddy flux, and observational tests. *J. Phys. Oceanogr.*, **38**, 29–43, https://doi.org/10.1175/2007JPO3671.1.

CATDS, 2017: CATDS-PDC L3OS 2Q - Debiased daily valid ocean salinity values product from SMOS satellite. CATDS (CNES, IFREMER, LOCEAN, ACRI), accessed 10 April 2018, https://doi.org/10.12770/12dba510-cd71-4d4f-9fc1-9cc027d128b0.

Cayula, J.-F., and P. Cornillon, 1992: Edge detection algorithm for SST images. *J. Atmos. Oceanic Technol.*, **9**, 67–80, https://doi.org/10.1175/1520-0426(1992)009<0067:EDAFSI>2.0.CO;2.

D'Asaro, E., C. Lee, L. Rainville, R. Harcourt, and L. Thomas, 2011: Enhanced turbulence and energy dissipation at ocean fronts. *Science*, **332**, 318–322, https://doi.org/10.1126/science.1201515.

Delcroix, T., and M. McPhaden, 2002: Interannual sea surface salinity and temperature changes in the western Pacific warm pool during 1992–2000. *J. Geophys. Res.*, **107**, 8002, https://doi.org/10.1029/2001JC000862.

——, M. J. McPhaden, A. Dessier, and Y. Gouriou, 2005: Time and space scales for sea surface salinity in the tropical oceans. *Deep-Sea Res. I*, **52**, 787–813, https://doi.org/10.1016/j.dsr.2004.11.012.

Desprès, A., G. Reverdin, and F. d'Ovidio, 2011a: Mechanisms and spatial variability of mesoscale frontogenesis in the northwestern subpolar gyre. *Ocean Modell.*, **39**, 97–113, https://doi.org/10.1016/j.ocemod.2010.12.005.

——, ——, and ——, 2011b: Summertime modification of surface fronts in the North Atlantic subpolar gyre. *J. Geophys. Res.*, **116**, C10003, https://doi.org/10.1029/2011JC006950.

Drucker, R., and S. C. Riser, 2014: Validation of Aquarius sea surface salinity with Argo: Analysis of error due to depth of measurement and vertical salinity stratification. *J. Geophys. Res. Oceans*, **119**, 4626–4637, https://doi.org/10.1002/2014JC010045.

Drushka, K., W. E. Asher, B. Ward, and K. Walesby, 2016: Understanding the formation and evolution of rain-formed fresh lenses at the ocean surface. *J. Geophys. Res. Oceans*, **121**, 2673–2689, https://doi.org/10.1002/2015JC011527.

Fahrbach, E., G. Rohardt, and R. Sieger, 2007: 25 years of Polarstern hydrography (1982–2007). WDC-MARE Rep. 5, 88 pp., https://doi.org/10.2312/wdc-mare.2007.5.

Fore, A. G., S. H. Yueh, W. Tang, B. W. Stiles, and A. K. Hayashi, 2016: Combined active/passive retrievals of ocean vector wind and sea surface salinity with SMAP. *IEEE Trans. Geosci. Remote Sens.*, **54**, 7396–7404, https://doi.org/10.1109/TGRS.2016.2601486.

Gaillard, F., D. Diverres, S. Jacquin, Y. Gouriou, J. Grelet, M. LeMenn, J. Tassel, and G. Reverdin, 2015: Sea Surface Salinity from French Research Vessels: Delayed mode dataset (updated annually). Subset used: 2001–2013. SEANOE, accessed 15 March 2018, http://doi.org/z79.

Henocq, C., J. Boutin, G. Reverdin, F. Petitcolin, S. Arnault, and P. Lattes, 2010: Vertical variability of near-surface salinity in the tropics: Consequences for L-band radiometer calibration and validation. *J. Atmos. Oceanic Technol.*, **27**, 192–209, https://doi.org/10.1175/2009JTECHO670.1.

Hosegood, P., M. C. Gregg, and M. H. Alford, 2006: Submesoscale lateral density structure in the oceanic surface mixed layer. *Geophys. Res. Lett.*, **33**, L22604, https://doi.org/10.1029/2006GL026797.

——, M. Gregg, and M. Alford, 2008: Restratification of the surface mixed layer with submesoscale lateral density gradients: Diagnosing the importance of the horizontal dimension. *J. Phys. Oceanogr.*, **38**, 2438–2460, https://doi.org/10.1175/2008JPO3843.1.

JAMSTEC, 2016: Data and Sample Research System for Whole Cruise Information in Japan Agency for Marine-Earth Science and Technology (DARWIN). Accessed 1 November 2016, http://www.godac.jamstec.go.jp/darwin/.

Kerr, Y. H., and Coauthors, 2010: The SMOS mission: New tool for monitoring key elements of the global water cycle. *Proc. IEEE*, **98**, 666–687, https://doi.org/10.1109/JPROC.2010.2043032.

Klein, P., and Coauthors, 2015: Mesoscale/sub-mesoscale dynamics in the upper ocean. CNES–NASA, https://swot.jpl.nasa.gov/documents.htm.

Kolodziejczyk, N., G. Reverdin, J. Boutin, and O. Hernandez, 2015: Observation of the surface horizontal thermohaline variability at mesoscale to submesoscale in the north-eastern subtropical Atlantic Ocean. *J. Geophys. Res. Oceans*, **120**, 2588–2600, https://doi.org/10.1002/2014JC010455.

Lagerloef, G., and Coauthors, 2010: Resolving the global surface salinity field and variations by blending satellite and in situ observations. *Proceedings of OceanObs'09: Sustained Ocean Observations and Information for Society*, J. Hall, D. E. Harrison, and D. Stammer, Eds., IOC/UNESCO, 11 pp., https://archimer.ifremer.fr/doc/00071/18216/.

Lapeyre, G., and P. Klein, 2006: Dynamics of the upper oceanic layers in terms of surface quasigeostrophy theory. *J. Phys. Oceanogr.*, **36**, 165–176, https://doi.org/10.1175/JPO2840.1.

Legal, C., P. Klein, A.-M. Treguier, and J. Paillet, 2007: Diagnosis of the vertical motions in a mesoscale stirring region. *J. Phys. Oceanogr.*, **37**, 1413–1424, https://doi.org/10.1175/JPO3053.1.

Lévy, M., P. Klein, and A.-M. Treguier, 2001: Impact of submesoscale physics on production and subduction of phytoplankton in an oligotrophic regime. *J. Mar. Res.*, **59**, 535–565, https://doi.org/10.1357/002224001762842181.

Lindstrom, E. J., J. B. Edson, J. J. Schanze, and A. Y. Shcherbina, 2019: SPURS-2: Second Salinity Processes in the Upper-ocean Regional Study—The Eastern Equatorial Pacific Experiment. *Oceanography*, **32** (2), 15–19, https://doi.org/10.5670/oceanog.2019.207.

MacKinnon, J. A., and Coauthors, 2016: A tale of two spicy seas. *Oceanography*, **29** (2), 50–61, https://doi.org/10.5670/oceanog.2016.38.

Maes, C., B. Dewitte, J. Sudre, V. Garçon, and D. Varillon, 2013: Small-scale features of temperature and salinity surface fields in the Coral Sea. *J. Geophys. Res. Oceans*, **118**, 5426–5438, https://doi.org/10.1002/jgrc.20344.

Manucharyan, G. E., and A. F. Thompson, 2017: Submesoscale sea ice-ocean interactions in marginal ice zones. *J. Geophys. Res. Oceans*, **122**, 9455–9475, https://doi.org/10.1002/2017JC012895.

Meissner, T., L. Ricciardulli, and F. J. Wentz, 2017: Capability of the SMAP mission to measure ocean surface winds in storms. *Bull. Amer. Meteor. Soc.*, **98**, 1660–1677, https://doi.org/10.1175/BAMS-D-16-0052.1.

——, F. Wentz, and D. Le Vine, 2018: The salinity retrieval algorithms for the NASA Aquarius Version 5 and SMAP Version 3 releases. *Remote Sens.*, **10**, 1121, https://doi.org/10.3390/rs10071121.

Menemenlis, D., C. Hill, G. Forget, C. H. B. Nelson, B. Ciotti, and A. Chaudhuri, 2014: Global llcXXXX simulations with tides. ECCO meeting presentation, http://ecco2.org/meetings/2014/Jan_MIT/presentations/ThursdayPM/05_menemenlis.pdf.

NASA Aquarius Project, 2017: Aquarius official release level 2 sea surface salinity and wind speed data V5.0. PO.DAAC, accessed 11 November 2018 https://doi.org/10.5067/AQR50-2SOCS.

Pietri, A., P. Testor, V. Echevin, A. Chaigneau, L. Mortier, G. Eldin, and C. Grados, 2013: Finescale vertical structure of the upwelling system off southern Peru as observed from glider data. *J. Phys. Oceanogr.*, **43**, 631–646, https://doi.org/10.1175/JPO-D-12-035.1.

Ramachandran, S., and Coauthors, 2018: Submesoscale processes at shallow salinity fronts in the Bay of Bengal: Observations during the winter monsoon. *J. Phys. Oceanogr.*, **48**, 479–509, https://doi.org/10.1175/JPO-D-16-0283.1.

Reverdin, G., S. Morisset, J. Boutin, and N. Martin, 2012: Rain-induced variability of near sea-surface T and S from drifter data. *J. Geophys. Res.*, **117**, C02032, https://doi.org/10.1029/2011JC007549.

Roemmich, D., and J. Gilson, 2009: The 2004-2008 mean and annual cycle of temperature, salinity, and steric height in the global ocean from the Argo program. *Prog. Oceanogr.*, **82**, 81–100, https://doi.org/10.1016/j.pocean.2009.03.004.

Rossby, T., 2001: Sustained ocean observations from merchant marine vessels. *Mar. Technol. Soc. J.*, **35**, 38–42, https://doi.org/10.4031/002533201788057873.

Rudnick, D. L., and R. Ferrari, 1999: Compensation of horizontal temperature and salinity gradients in the ocean mixed layer. *Science*, **283**, 526–529, https://doi.org/10.1126/science.283.5401.526.

——, and J. P. Martin, 2002: On the horizontal density ratio in the upper ocean. *Dyn. Atmos. Oceans*, **36**, 3–21, https://doi.org/10.1016/S0377-0265(02)00022-2.

Sena Martins, M., N. Serra, and D. Stammer, 2015: Spatial and temporal scales of sea surface salinity variability in the Atlantic Ocean. *J. Geophys. Res.*, **120**, 4306–4323, https://doi.org/10.1002/2014JC010649.

Shcherbina, A. Y., E. A. D'Asaro, S. C. Riser, and W. S. Kessler, 2015: Variability and interleaving of upper-ocean water masses surrounding the North Atlantic salinity maximum. *Oceanography*, **28**, 106–113, https://doi.org/10.5670/oceanog.2015.12.

Smith, S., J. Rolph, K. Briggs, and M. Bourassa, 2009: Quality-Controlled Underway Oceanographic and Meteorological Data from the Center for Ocean-Atmospheric Predictions Center (COAPS)–Shipboard Automated Meteorological and Oceanographic System (SAMOS). NOAA/NCEI, accessed 1 September 2017, https://doi.org/10.7289/v5qj7f8r.

Soloviev, A., and R. Lukas, 1997: Sharp frontal interfaces in the near-surface layer of the ocean in the western equatorial Pacific warm pool. *J. Phys. Oceanogr.*, **27**, 999–1017, https://doi.org/10.1175/1520-0485(1997)027<0999:SFIITN>2.0.CO;2.

Tang, W., S. H. Yueh, A. G. Fore, and A. Hayashi, 2014: Validation of Aquarius sea surface salinity with in situ measurements from Argo floats and moored buoys. *J. Geophys. Res. Ocean*, **119**, 6171–6189, https://doi.org/10.1002/2014JC010101.

——, and Coauthors, 2017: Validating SMAP SSS with in situ measurements. *Remote Sens. Environ.*, **200**, 326–340, https://doi.org/10.1016/j.rse.2017.08.021.

Thomas, L. N., A. Tandon, and A. Mahadevan, 2008: Submesoscale processes and dynamics. *Ocean Modeling in an Eddying Regime*, *Geophys. Monogr.*, Vol. 177, Amer. Geophys. Union, 17–38.

Thompson, A. F., A. Lazar, C. Buckingham, A. C. Naveira Garabato, G. M. Damerell, and K. J. Heywood, 2016: Open-ocean submesoscale motions: A full seasonal cycle of mixed layer instabilities from gliders. *J. Phys. Oceanogr.*, **46**, 1285–1307, https://doi.org/10.1175/JPO-D-15-0170.1.

Vinogradova, N. T., and R. M. Ponte, 2013: Small-scale variability in sea surface salinity and implications for satellite-derived measurements. *J. Atmos. Oceanic Technol.*, **30**, 2689–2694, https://doi.org/10.1175/JTECH-D-13-00110.1.